Journal of Materials Chemistry C

ROYAL SOCIETY OF CHEMISTRY

PAPER

View Article Online
View Journal | View Issue

Cite this: J. Mater. Chem. C, 2024, 12, 11550

Interrogating the CISS effect in chiral and paramagnetic organic radicals: the impact of the molecular spin over the total spin polarization†

J. Alejandro De Sousa, [ab] Paula Mayorga-Burrezo,[a] Sandra Míguez-Lago, [c] José Catalán-Toledo, [a] Raúl Ramos-Tomás,[a] Ana Ortuño,[c] Linda A. Zotti, [def] Juan José Palacios,[efg] Araceli G. Campaña, *[c] Jaume Veciana *[a] and Núria Crivillers *[a]

Continuous research on new chiral molecular materials brings new exciting properties to the field of molecular electronics. The discovery of the chirality-induced spin selectivity (CISS) effect has expanded the list of applications for chiral structures, opening promising avenues for their exploitation in molecular spintronics. In this work, the persistent propeller-like organic perchlorotriphenylmethyl (PTM) radical is investigated as a potential spin filter combining chirality and paramagnetism. In particular, two different PTM derivatives, mono- and bis-functionalized, with one or two terminal alkyne groups have been used for the preparation of enantioenriched solid-state assemblies. The analysis of their chiroptical properties reveals that the functionalization does not play a crucial role in their final conformational stability and highlights the dissimilarities of the racemization barriers in solution and solid states. Spin-dependent electrochemical and charge transport measurements of enantioenriched PTM-based self-assembled monolayers did not reveal the existence of the CISS effect. Density functional theory quantum transport calculations show that the most dominant contribution to the spin polarization would not be CISS-related polarization, but the one intrinsically associated with the radical spin. Nevertheless, at room temperature this contribution is affected by thermal fluctuations averaging to a net zero spin polarization.

Received 4th April 2024,
Accepted 17th June 2024

DOI: 10.1039/d4tc01389a

rsc.li/materials-c

1. Introduction

Chirality is an intrinsic property of some synthetic molecules,[1] biomolecules[2] and (nano)materials,[3–5] determined by the spatial arrangement of the atoms in their structures. In this sense, left- and right-handed mirror images of chiral systems are non-superimposable, defining their specific activity or function. Therefore, chirality is widely recognized as an area of scientific and technological interest with a high impact in different fields, such as biomedicine, (bio)molecular sensing, and asymmetric catalysis,[5–11] and also great potential for new emerging applications in the molecular electronics and quantum technology fields.[12–14]

Two main approaches have traditionally been followed to obtain chiral (nano)materials: (i) transferring the chiral activity of molecules to achiral structures or materials (such as nanoparticles,[15] quantum dots,[3,16] nanographenes,[17] and nanostructured surfaces through assembled monolayer formation, both physisorbed or chemisorbed[18–20]) and (ii) inducing chiral conformation using chiral and achiral building blocks to generate supramolecular chiral materials, like liquids[21] or twisted crystals[22] as well as nanofibers.[23] Overall, they display appealing optical, electrochemical and optoelectronic properties, which can be exploited for instance as templates for efficient enantiomeric separation and recognition[24–26] or to modify the charge

[a] Institut de Ciència de Materials de Barcelona (ICMAB, CSIC), Campus de la UAB s/n, Bellaterra, 081093, Spain. E-mail: ncrivillers@icmab.es, vecianaj@icmab.es
[b] Laboratorio de Electroquímica, Departamento de Química, Universidad de los Andes, Facultad de Ciencias, Mérida, 5101, Venezuela
[c] Departamento de Química Orgánica, Universidad de Granada and Unidad de Excelencia en Química (UEQ), Avda. Fuentenueva s/n, Granada, 18071, Spain. E-mail: araceligc@ugr.es
[d] Departamento de Física Teórica de la Materia Condensada, Universidad Autónoma de Madrid, Cantoblanco, 28049, Spain
[e] Institute of Condensed Matter Physics (IFIMAC), Universidad Autónoma de Madrid, Cantoblanco, 28049, Spain
[f] Nicolás Cabrera Institute, Universidad Autónoma de Madrid, Cantoblanco, 28049, Spain
[g] Departamento de Física de la Materia Condensada, Universidad Autónoma de Madrid, Cantoblanco, 28049, Spain

† Electronic supplementary information (ESI) available: Detailed experimental procedures for enantiomeric resolution, chiroptical characterization, and substrate and SAM preparation and characterization. See DOI: https://doi.org/10.1039/d4tc01389a

transport in organic-based electronic devices, *e.g.* the current density or charge carrier mobility in molecular junctions or in organic field-effect transistors, respectively.[27] It has been proved that chiral materials have the ability to modulate the charge transport of spin-polarized electrons through self-assembled structures, acting as spin filters. This phenomenon was defined as the chirality-induced spin selectivity (CISS) effect by R. Naaman's group.[28–31] CISS is a revolutionary effect in molecular (spin)electronics,[32–34] having been also used to explain different phenomena in chiral recognition/separation[35,36] and spin-controlled chemical reactions.[37,38] To date, several experimental approaches have been followed to measure the CISS effect in films and in monolayers: (i) by optical means,[39,40] (ii) charge transport through chiral materials,[41,42] (iii) electrochemical experiments[43] and (iv) magnetoresistance[42,44] and Hall-effect measurements.[45]

Persistent organic radicals are very appealing candidates for molecular electronics and spintronics, which can combine redox, optical, chiral and magnetic activities.[46] Some examples of organic radicals that combine paramagnetism and chirality are based on cationic radical bicarbazoles,[47] hetero[4]helicene radical cations,[48] α-nitronyl nitroxide radicals,[49] and trityl based radicals,[50–54] among which, the perchlorotriphenyl methyl (PTM) radical derivatives have emerged as promising candidates for many applications thanks to their persistence and thermochemical stability.[55]

Having a D_3 symmetry, the PTM radical is obtained as a racemic mixture of minus (*M*) and plus (*P*) enantiomers, depending on the torsion sense of the three phenyl rings protecting the odd electron in the central sp^2 α-carbon.[55] (*P*)- and (*M*)-atropisomers of PTM derivatives can be isolated using chiral stationary phase chromatographic methods[53,56] and their presence in films prepared by vacuum sublimation has been previously revealed by STM studies.[57] Additionally, some of us have recently reported the first description of organic free trityl radicals as intrinsic circularly polarized luminescence emitters.[53,54]

Towards practical applications, the surface deposition of racemic PTM radical derivatives has been realized on several substrates (metallic, metal-oxides and carbonaceous) to explore their multifunctional properties[58–60] and stability.[61] In two-terminal molecular junctions, it has been demonstrated that the better level alignment of the SUMO orbital (single-unoccupied molecular orbital) of PTM derivatives with the Fermi level of the metallic top-contact electrode largely influences the charge transport, enhancing the tunneling current up to two orders of magnitude in comparison with the closed-shell derivative. This has been observed in different junction configurations, either in metal/PTM-based monolayer/metal[62–64] or in metal/PTM-based monolayer/semiconductor.[65] Nevertheless, the implications on spin filtering of homochiral PTM radicals

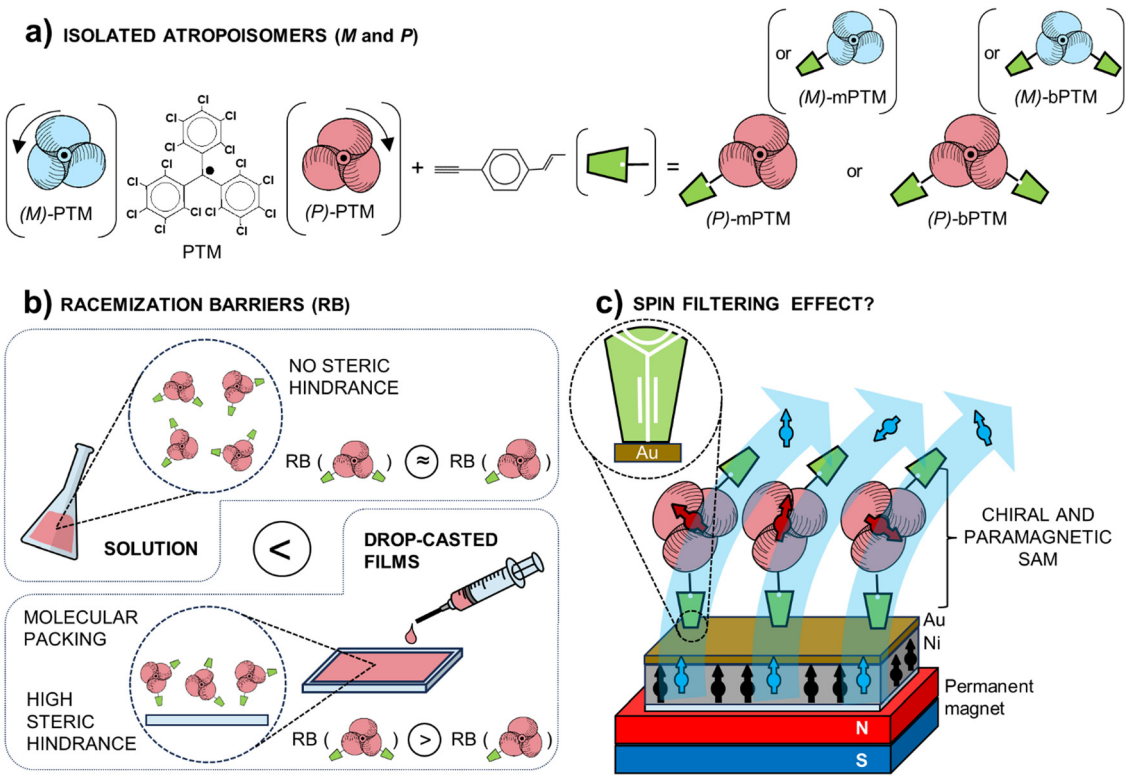

Scheme 1 Schematic representation of (a) the isolated atropisomers (*i.e.*, plus (*P*)- or minus (*M*)-) of the mono- and bis-functionalized PTM radicals, **mPTM** and **bPTM**, respectively. See Scheme S1 in the ESI† for further details; (b) steric hindrances of **(*P*)-mPTM** and **(*P*)-bPTM** in solution and as drop-cast films, responsible for the differences in their racemization barriers (RB); (c) self-assembled monolayers (SAM) of **(*P*)-bPTM** to study the spin-transport. Both, (*M*)- and (*P*)-atropisomers were considered during the experimental measurements reported in this work. Nonetheless, only (*P*)-derivatives are depicted in (b) and (c) for the sake of clarity.

deposited or grafted on surfaces are yet unexplored. To this end, functionalization with adequate anchoring groups would be required.

In this work, the chiroptical properties and conformational stability of two PTM radical derivatives, in solution and solid states (as drop-cast films), are discussed in terms of their functionalization. With this aim, PTM radical derivatives having one (mono-functionalized, **mPTM**) or two (bis-functionalized, **bPTM**) terminal alkyne groups in the form of 4-ethynylstyryl substituents (Scheme 1) are investigated. The terminal alkyne groups were selected as they allow the preparation of self-assembled monolayers (SAMs) on gold substrates through the formation of a C–Au bond.[66–69] Thus, enantiomerically enriched paramagnetic SAMs have been prepared and characterized to interrogate the CISS effect. To this end, spin-dependent electrochemical and charge transport measurements of PTM SAMs in metal/monolayer/metal junctions under a magnetic field have been carried out for the first time. The lack of spin polarization found in the experimental results has been rationalized by density functional theory quantum transport calculations.

2. Results and discussion

2.1. Enantiomeric resolution of chiral PTM radical derivatives

mPTM and **bPTM** (Scheme 1a and Scheme S1, ESI†) were synthesized following a previously reported procedure.[64] After a full characterization of the racemic mixtures (see ESI,† Fig. S1) their enantiomeric resolution was achieved using high-performance liquid chromatography (HPLC) equipped with chiral stationary phases (CSP),[70–75] yielding enantioenriched samples (Fig. 1).

Indeed, enantioenriched solutions with an enantiomeric excess higher than 86% were obtained in both cases (see ESI,† Fig. S2). Then, after solvent evaporation at low temperature the enantioenriched products were stored at −20 °C to ensure their stability, and then they were used for the experiments described below.

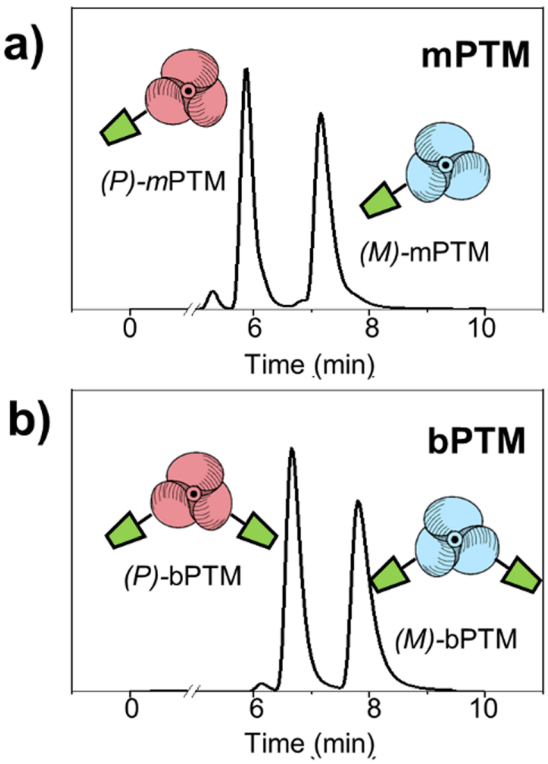

Fig. 1 (CSP)-HPLC chromatograms of: (a) **mPTM** and (b) **bPTM**. Retention times: 5.87 and 7.15 min for the **(*P*)-** and **(*M*)-mPTM**, respectively, and 6.67 and 7.80 min in the case of **(*P*)-** and **(*M*)-bPTM**, respectively.

2.2. Chiroptical properties and enantiomerization barriers: solution *vs.* solid state

The absolute configurations of the propeller-like enantiomeric forms of **mPTM** and **bPTM** radicals were evaluated by electronic circular dichroism (ECD). Fig. 2a and b depict the typical ECD mirror image spectra of (*M*)- and (*P*)-enantiomers in toluene of both radicals. The ECD spectra show two main bands for **mPTM**, around 339 nm ($\Delta\varepsilon$ = 8.7 M^{-1} cm^{-1}) and 388 nm ($\Delta\varepsilon$ = 16.8 M^{-1} cm^{-1}), in line with the characteristic UV-vis absorption spectra (see Fig. 2c). Similar features at 340 nm ($\Delta\varepsilon$ = 6.0 M^{-1} cm^{-1}) and 415 nm (broadband, $\Delta\varepsilon$ = 7.1 M^{-1} cm^{-1}) appeared in the case of **bPTM**. The absorption anisotropy factors, $|g_{abs}|$, were estimated for the two compounds and normalized by their enantiomeric excess (ee), as $|g_{abs}|$/ee (Fig. 2d). In this sense, $|g_{abs}|$/ee values of 7.5 × 10^{-4} (**mPTM**, at 388 nm) and 5.8 × 10^{-4} (**bPTM**, at 394 nm) were estimated. Additionally, the assignment of the absolute configuration for each pair of enantiomers was done through comparison with DFT-computed UV-vis and ECD spectra employing different functionals and basis sets (see ESI† Section S3).

The results are in good agreement with previous reports on other propeller-like trityl radical analogues,[53,54] where the negative Cotton effect in the most intense electronic transitions and the positive Cotton effect at the lowest energetic transition were associated with (*P*)-configurations.

The evolution of the ECD spectra at different temperatures was measured to determine the kinetics of the racemization processes in solution. A linear regression was used to fit the decay of the main ECD feature at different temperatures, assuming first-order kinetics (see Fig. S4 and Table S1, ESI†). On the other hand, the enantiomerization barrier ($\Delta G^{\ddagger}$, Table S2, ESI†) was estimated by means of the Eyring–Polanyi (eqn (S3) and Fig. S6, ESI†) and Gibbs equations (eqn (S5), ESI†). Moreover, kinetic parameters at different temperatures were also determined measuring the decay of the enantiomeric excess by the dynamic (CSP)-HPLC method[76] to corroborate the results obtained with ECD (see Fig. S5 and Table S1, ESI†). Interestingly, identical $\Delta G^{\ddagger}$ = 22 kcal mol^{-1} (Table S2, ESI†) was estimated for the enantiomers of **mPTM** and **bPTM**, following the two approaches, in good agreement with the previous reports on other PTM radicals.[53,54,56,77] The similarity of the barrier values for the (*M*)- and (*P*)- enantiomers is an indication of the symmetry of the barrier, which is a prerequisite to use a transition coefficient of 0.5 in the Eyring–Polanyi equation.[78–81]

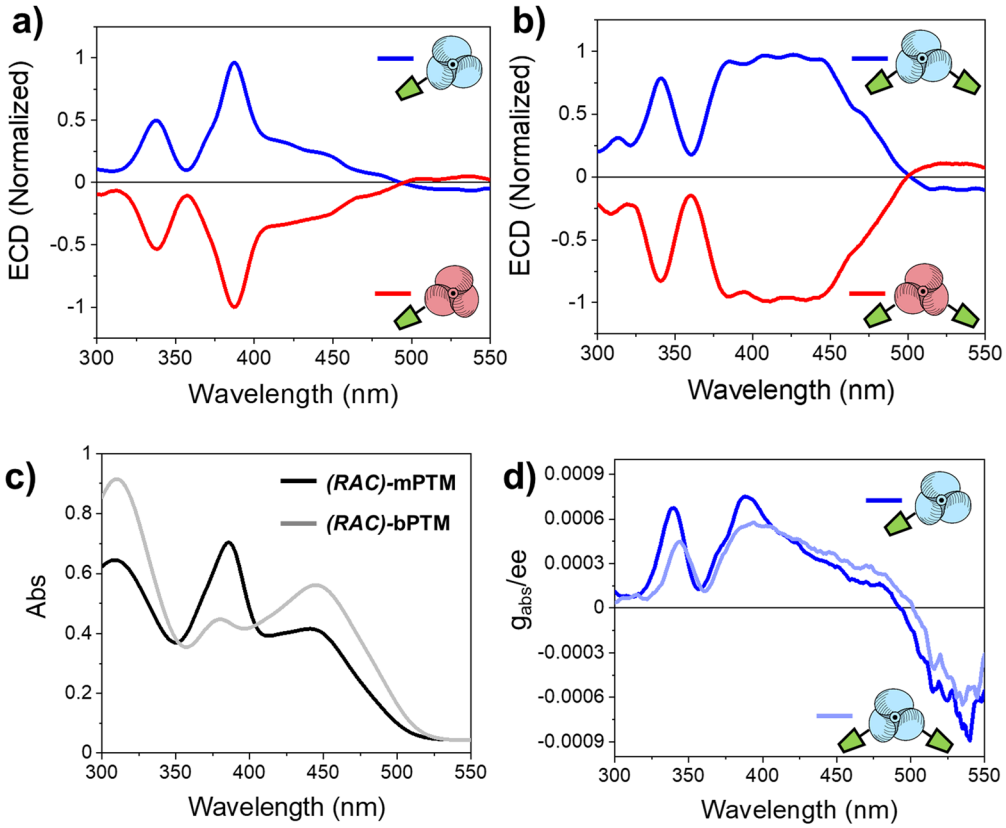

Fig. 2 ECD spectra of (*P*)- (red) and (*M*)-(blue) enantiomers of: (a) **mPTM** and (b) **bPTM** in solution. Concentration ≈ 50 μM; solvent = toluene; T = 273 K; (c) UV-vis electronic absorption spectra of the racemic (*RAC*) mixtures of **mPTM** (black) and **bPTM** (gray) in toluene (concentration ≈ 30 μM); (d) absorption anisotropy factors (g_{abs}/ee) of ***(M)*-mPTM** (blue) and (*M*)-bPTM (light blue). Concentration ≈ 50 μM; solvent = toluene; T = 288 K.

The $\Delta G^{\ddagger}$ value of 22 kcal mol^{-1} is similar to those previously reported for PTM analogues, suggesting a similar enantiomerization mechanism based on a two-blade flip, which is the lower-lying pathway for conformational equilibrium. Thus, considering the plane formed by the three-carbon bridge atoms (carbons linked to the αC), two phenyl rings turn in the same sense achieving a perpendicular position with respect to this plane, while a third one rotates in the opposite sense changing the side.[51,82] In summary, no effect of the mono- or bis-functionalization of the PTM radical (**mPTM** and **bPTM**, respectively) was observed in their interconversion barriers, probably because their functionalization is located at the *para*-position with respect to the αC, which does not create an effective steric hindrance and does not have a significant influence on the electronic conjugation with the unpaired electron to alter the energy barrier either.

Numerous techniques have been developed to prepare thin films of organic molecules: *e.g.* thermal evaporation under vacuum control, drop-casting, spin-coating, inject printing and solution shearing.[58,83–85] However, in the case of solution processes, room temperature or higher is usually required for solvent evaporation. It has been demonstrated that the enantiomers of **mPTM** and **bPTM** undergo a racemization process above 278 K, with an estimated half-life time higher than 20 min at 298 K (see ESI;† Table S1). Because of this, enantiomeric solutions in a low-boiling point solvent, like dichloromethane (DCM), were prepared and drop-cast (50 μL; 1 mM) at 273 K on transparent substrates (quartz/Ti (2 nm)/Au (6 nm)). Quick evaporation of the solvent under vacuum was performed to preserve the ee in the thin films. Following this methodology, translucent films were obtained allowing further spectroscopic characterization. First, by optical microscopy only wave-valley structures typically formed during rapid solvent evaporation, like DCM, were observed (Fig. S7, ESI†). Tapping-mode atomic force microscopy (AFM) was used to scan the surface topography (avoiding the regions with aggregates, Fig. S8, ESI†). The formation of non-continuous but quite homogenous films was revealed in most of the cases except for the **(*P*)-bPTM**-film, where more defects and small aggregates were detected. Furthermore, XRD analysis was performed showing an amorphous-microcrystalline structure with many surface irregularities (Fig. S9 (ESI†)).

Importantly, the paramagnetic character of the resulting films was proved by EPR (Fig. 3a). The obtained spectra are in good agreement with the ones measured in solution, with a g-value of 2.0022, like that of free electrons indicating a null spin orbit coupling. However, their line width (1.80 G) is higher than the one obtained in solution (1.1–1.2 G), preventing the observation of the hyperfine coupling lines (see Fig. S1b, ESI†). This behavior is usually ascribed to molecules without a free

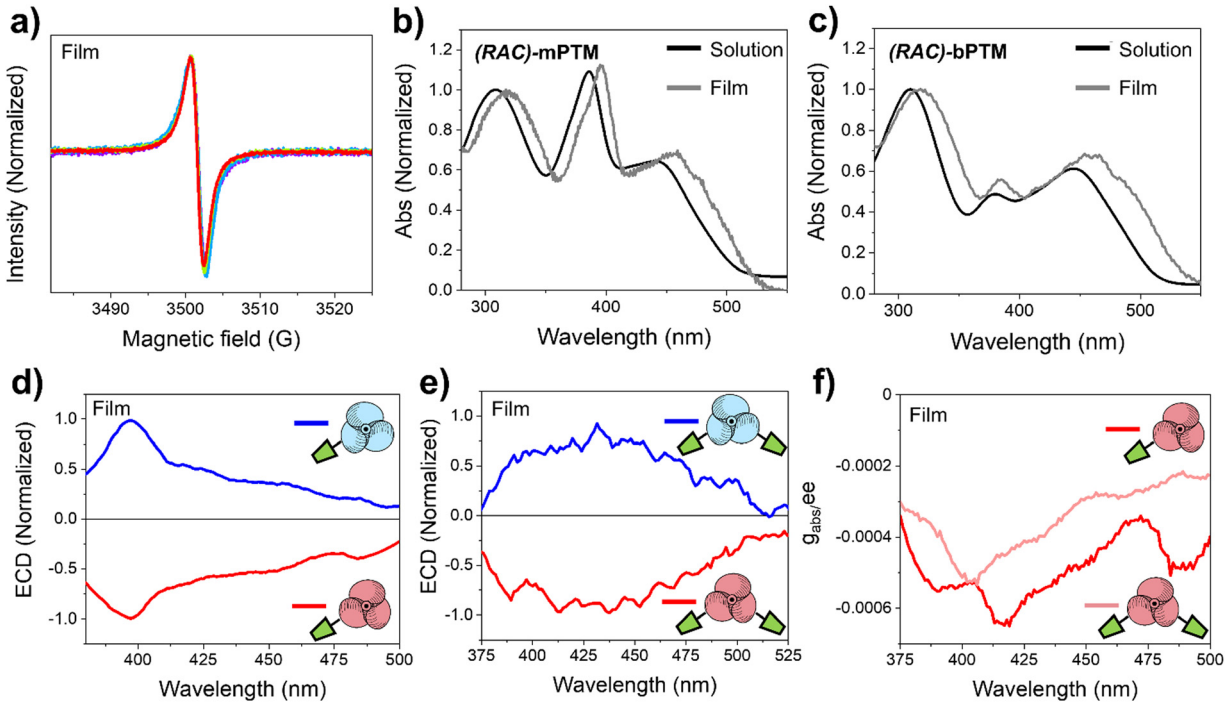

Fig. 3 Spectroscopic characterization of the enantioenriched films deposited by drop-casting on Au/quartz substrates. (a) EPR spectra of the **(*P*)-mPTM-film** (violet), **(*M*)-mPTM-film** (blue), **(*P*)-bPTM-film** (green) and **(*M*)-bPTM-film** (red); normalized UV-vis spectra in a toluene solution (black) and film (grey) for the racemic (*RAC*)-mixtures of: (b) **mPTM** and (c) **bPTM**; ECD spectra of: (d) **(*P*)-mPTM-film** (red), **(*M*)-mPTM-film** (blue); and (e) **(*P*)-bPTM-film** (red) and **(*M*)-bPTM-film** (blue); (f) absorption anisotropy factor normalized by the enantiomeric excess (g_{abs}/ee) for **(*P*)-mPTM-film** (red) and **(*P*)-bPTM-film** (light-red) at room temperature.

rotation (or with a slow tumbling or not tumbling at all) as for a solid compound with restricted rotations. Furthermore, small red-shifted electronic absorption spectra were obtained for the racemic (*RAC*) mixtures of **mPTM** and **bPTM** (Fig. 3b and c and Table S3, ESI†) when moving from solution to thin films, which might be associated with a certain molecular aggregation in the solid state.[86]

Finally, the chiroptical properties of the thin films were evaluated (Fig. 3d and e). When compared with the ECD results from the samples in solution, the same features were found in thin films, with mirror image spectra of (*M*)- and (*P*)-enantiomers. As in UV-vis electronic absorption data, red-shifted ECD bands were obtained in the case of thin films. The absorption anisotropy factors normalized by the enantiomeric excess (g_{abs}/ee) were also estimated (Fig. 3f), obtaining values of 5.5×10^{-4} for **(*P*)-mPTM-film** (at 390 nm) and 5.3×10^{-4} for **(*P*)-bPTM-film** (at 404 nm). Importantly, similar g_{abs}/ee values resulted from the comparison between solution and thin films in both cases, meaning that the chiroptical properties were preserved in the solid state.

ECD measurements at different temperatures (295–333 K) were run to evaluate the stability of the PTM-enantiomers in the solid state. Remarkably, no significant changes associated with the deposited material were observed in the ECD spectra of the enantioenriched films at 295 K for one hour (Fig. 4). This result points to a higher conformational stability of the radicals in the thin films than in solution (Fig. S4c and S4f, ESI†). Hence, higher temperatures (313–333 K) were selected to address the conformational stability of the films employing ECD (Fig. S10, ESI†). Interestingly, a 3 times higher half-life time at 313 K was determined for the **(*M*)-mPTM-film**, with respect to the one obtained in solution at 298 K (see Table S1, ESI†). In the case of the **(*P*)-bPTM film**, no evolution was detected for 1.5 hours in the ECD spectra recorded at 313 K and even at 333 K (Fig. S10d and e, ESI†).

An enantiomerization barrier equal to 24 kcal mol^{-1} was estimated for the **(*M*)-mPTM-film** (Fig. S11, ESI†). Remarkably, this value is in agreement with the barrier reported for other stable enantiomers, such as Finland trityl radicals[51,82] or carbo[5]helicenes.[87,88] On the other hand, it is on average 2 kcal mol^{-1} higher than what was found in solution. This increase might be likely thanks to the molecular rotation restrictions of the propeller-like structure by virtue of the lateral interactions occurring in the solid state due to the molecular packing. Additionally, no racemization barrier could be determined for the **(*P*)-bPTM-film** due to the high stability observed even at 333 K for 1.5 hours. Therefore, a minimum value for the barrier of $\Delta G^{\ddagger} \geq$ 24 kcal mol^{-1} at 313 K was estimated using eqn (S13) (ESI†).[81] This higher conformational stability of the **bPTM-film** with respect to the **mPTM-film** might be associated with a higher steric hindrance effect imparted by the second functionality. This would promote a different spatial organization within the film, hampering the free rotation of the central perchlorophenyl rings. Overall, the obtained results clearly indicate that both **mPTM** and **bPTM** radicals are conformationally more stable in the solid state, as drop-cast films, than in solution.

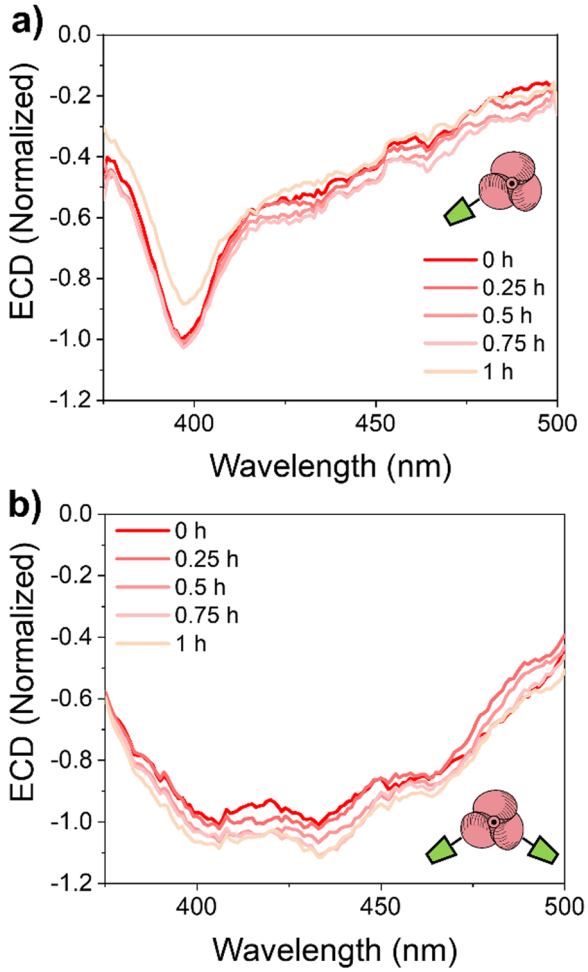

Fig. 4 Experimental ECD spectra of the enantioenriched films deposited by drop-casting on Au/quartz for: (a) **(*P*)-mPTM-film** and (b) **(*P*)-bPTM-film** at 295 K.

2.3. Enantioenriched PTM-based self-assembled monolayers

(*M*)- and (*P*)-enantiomers of **bPTM** were chosen to prepare SAMs based on their higher conformational stability (Fig. S12, ESI†). The grafting procedure for the SAM preparation was optimized following previous reports with some modifications (mainly decreasing temperature during the incubation) to guarantee the stability of the molecules. First, the procedure was tested using the racemic mixture of **bPTM** (*i.e.*, **(*RAC*)-bPTM-SAM**) (see ESI† for further details)[61,64,66] on gold surfaces (Au^{TS}, Fig. S13, ESI†). Fig. S14a (ESI†) shows the CV obtained for the **(*RAC*)-bPTM-SAM** prepared at low temperature at different scan rates, showing a reversible redox peak ascribed to the PTM (radical) ↔ PTM (anion) redox process at around $E_{1/2}$ = −0.71 V (*vs.* Fc/Fc^{+}). Moreover, up to 40 consecutive cycles at 0.1 V s^{-1} were run to prove its electrochemical stability (Fig. S14b, ESI†). No significant variation of the current density at the cathodic (J_{pc}) and anodic (J_{pa}) redox peaks was observed throughout the experiment, confirming the robust molecular confinement of **(RAC)-bPTM-SAM** and the stability of its radical character under electrochemical conditions. The linear regression of J_{pa} and J_{pc} *vs.* scan rate (Fig. S15a, ESI†) and the $I_{pa}/I_{pc} \approx 1$ (Fig. S15b, ESI†) evidenced the molecular surface confinement and the reversibility of the redox process. Moreover, a $\Delta E = E_{pa} - E_{pc}$ near zero (*i.e.*, 5–7 mV) at low scan rates was obtained, in line with an adsorbed redox reversible system without diffusional processes (Fig. S15c (red line), ESI†).[89,90] On the other hand, lateral molecular interactions within the SAM were suggested by the evolution of the full width at half maximum (FWHM) value at different scan rates. Considering FWHM = 3.53 RT/nF when no lateral interactions between the redox centers occur, the dissimilarities in Fig. S15c (ESI†) (blue line) suggested the existence of electrostatic effects among neighboring charged species suggesting a dense radical grafting.[89,90] Finally, a surface coverage of 3.1×10^{-11} mol cm^{-2} was determined from the area under the redox peak.[89,90]

Similar procedures were followed in the case of the enantioenriched **(*P*)-bPTM-SAM** and **(*M*)-bPTM-SAM** (see the scheme in Fig. 5a). The grafting was carried out on transparent Au surfaces with the same structure used for the thin films (quartz/$Ti_{(2nm)}/Au_{(6nm)}$) and using solutions with ee > 80%. CSP-HPLC analysis of the enantioenriched solution used for the grafting process before and after the SAM incubation was conducted to prove the preservation of the ee. In fact, a decrease of only 4–8% in the ee value was determined after the SAM preparation. The CV response in both cases showed the characteristic peak for a reversible PTM (radical) ↔ PTM (anion) redox process (Fig. 5b and c), proving their successful grafting with a surface coverage of 2.0×10^{-11} and 1.3×10^{-11} mol cm^{-2} for **(*P*)-bPTM-SAM** and **(*M*)-bPTM-SAM**, respectively. Unfortunately, no chiroptical responses could be acquired for the SAMs, in line with the low radical molecular population present in a single molecular monolayer. Nonetheless, considering the high conformational stability proved for **bPTM** drop-cast films and the low racemization of the enantioenriched solutions during the SAM preparation, these results were taken as indirect parameters to indicate the successful formation of enantioenriched SAMs.

2.4. Spin-dependent filtering effect of chiral PTM radical-based SAMs

As a first approach to investigate the effect on spin transport through a chiral PTM radical-based SAM, room temperature spin-dependent CV measurements were performed in line with previous reports.[44] A custom-built electrochemical cell was designed to guarantee close contact between the permanent magnet (field strength H = 0.4 T) and the SAMs acting as the working electrode (WE). This geometry allowed the easy flipping of the magnet side turning "up" and "down" the direction of the magnetization or *vice versa* without affecting the cell setup configuration (see Fig. S16, ESI†). Enantioenriched SAMs with the **bPTM** radical were grown on thermally evaporated ferromagnetic substrates (NiAu) for the electrochemical studies (see ESI† for further details on the substrate preparation). The CV response was analyzed in terms of the redox peak associated with the PTM (radical) ↔ PTM (anion) process (Fig. S17, ESI†) or following the electrochemical response of a redox probe[91] ($K_4Fe(CN)_6/K_3Fe(CN)_6$) in the solution (see Fig. S18, ESI†). In these two cases, no variations in the current density were observed when the spatial direction of the magnetic field

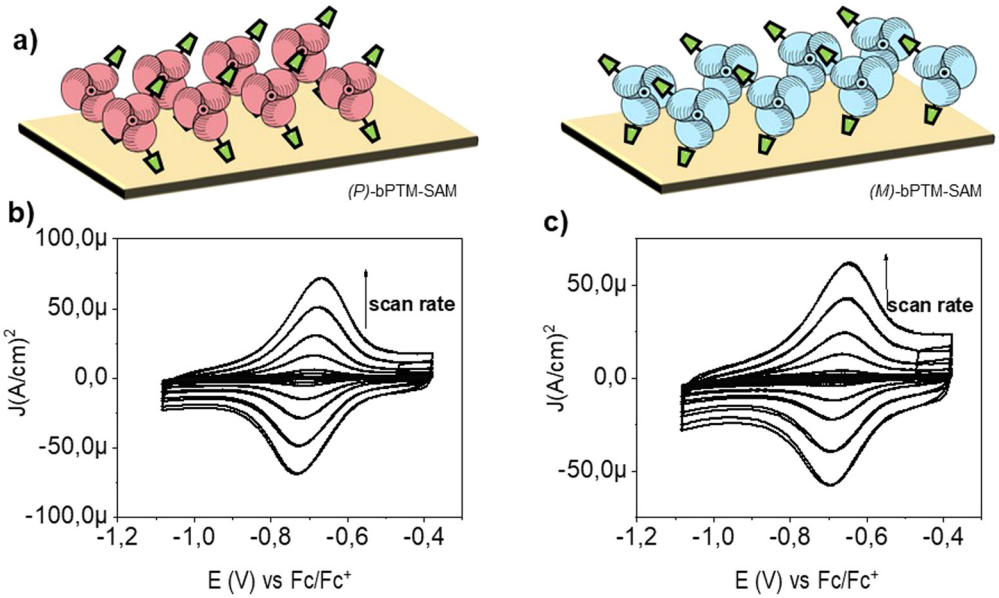

Fig. 5 (a) SAMs schematic representation and cyclic voltammetry of the enantioenriched (b) **(*P*)-bPTM-SAM** and (c) **(*M*)-bPTM-SAM** grafted on ($Au_{(6nm)}$/$Ti_{(2nm)}$/quartz) at different scan rates. Experimental conditions: CH_2Cl_2 + 0.2 M Bu_4NPF_6; scan rates: 0.05, 0.1, 0.25, 0.5, 1, 2, 3 and 4 V s^{-1}; Ar atmosphere. WE = SAMs/Au, RE = Ag wire (*vs.* Fc/Fc^+ couple), CE = Pt mesh.

vector was inverted, thus not displaying any signature of the occurrence of the CISS effect.

Based on these results and taking into account that the CISS phenomenon is a local effect, further evidenced when measuring the charge transport through an ordered chiral material, the enantioenriched **(*M*)-** and **(*P*)-bPTM-SAMs** were investigated in molecular junctions using an eutectic gallium-indium alloy (EGaIn) tip as a top contact electrode, in line with previous reports.[92] This technique has been scarcely employed for this purpose, with the work on SAMs of metallopeptides (TbLBTC and YLBTC) on NiAu substrates being the only one reported so far, to the best of our knowledge.[92] In the present work, we perform a similar study but using a chiral paramagnetic radical molecule[62–65] that shows a negligible magnetic anisotropy compared to the paramagnetic helical Tb-binding peptide.

For the electrical characterization, a permanent magnet (H = 0.4 T) was placed underneath the enantioenriched **bPTM-SAMs** prepared on template-stripped $NiAu^{TS}$ (see ESI† for further details, Fig. S19).[93,94] The monolayers were then softly top-contacted with a cone-shaped EGaIn tip. As shown in Fig. 6 for the $NiAu^{TS}$/**(*P*)-bPTM-SAM**//GaO_x/EGaIn junction and Fig. S20 (ESI†) for the $NiAu^{TS}$//**(*M*)-bPTM-SAM**//GaO_x/EGaIn junction, good reproducibility of the *JV* curves was observed, with junction yield formation higher than 70% (see Table S5, ESI†). Neither **(*P*)-bPTM-SAMs** nor **(*M*)-bPTM-SAMs** display any difference in the current density depending on the magnetic field orientation, as seen in Fig. 6 and Fig. S20 (ESI†).

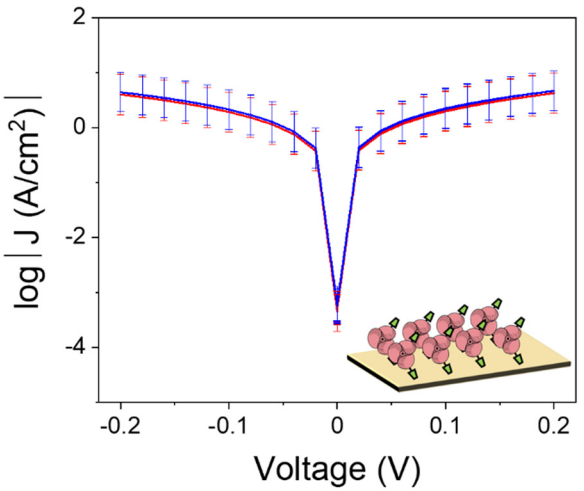

Fig. 6 Semilog plot of current density (J) *vs.* voltage (V) for the $NiAu^{TS}$/**(*P*)-bPTM-SAM**//GaO_x/EGaIn junction. Experiments with magnet "up" (red) and "down" (blue).

2.5. Theoretical calculations

Theoretical calculations based on the nonequilibrium Green's functions (NEGF) approach, as successfully done previously for other systems,[95–97] (Section S8 in the ESI†) were carried out to shed light on the lack of CISS effect observation. With this aim, a junction comprising **bPTM** between two gold clusters was considered, as shown in Fig. 7a. A spin–orbit-coupling (SOC) correction was included in the calculations to evaluate the potential of this system for exhibiting the CISS effect. Fig. 7b depicts the corresponding electrical transmission and spin polarization obtained at zero bias. The latter was calculated as:

$$P = T\uparrow\uparrow + T\uparrow\downarrow - T\downarrow\downarrow - T\downarrow\uparrow$$

where each term corresponds to the transmission calculated for all possible combinations of initial and final directions of the

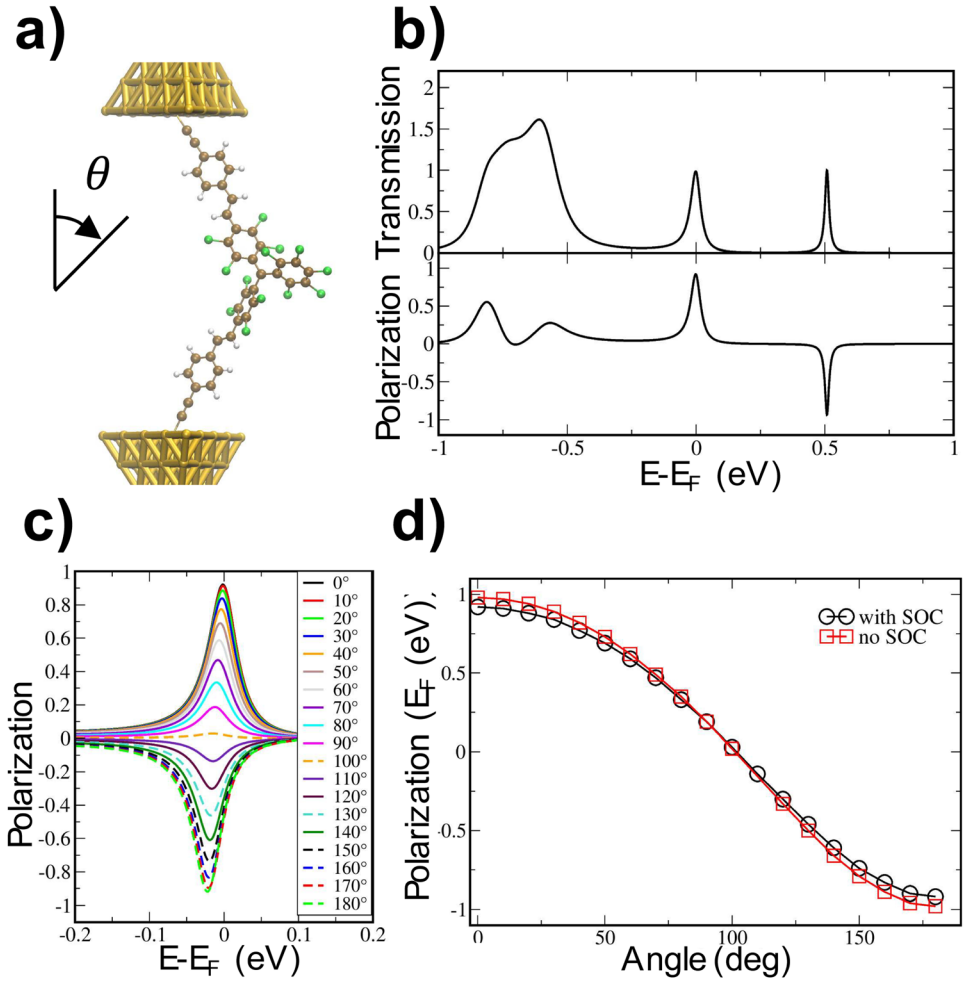

Fig. 7 (a) Geometrical structure of the Au–bPTM–Au junction studied theoretically; (b) transmission (top panel) and spin polarization (lower panel) as a function of bias, as obtained with a polar angle of 0°; (c) zoomed-in view of the spin polarization at the Fermi level for different polar angles of the direction of the radical spin; (d) maximum height of the polarization peak at the Fermi level with (black circles) and without (red squares) spin–orbit-coupling correction.

travelling spin for a given choice of the quantization axis (the transport direction here). SOC is only significant for Au atoms but, as shown in previous works,[95–97] it gives rise to spin polarization. This is particularly so below the Fermi level, but also at the Fermi level if a molecular orbital lies in the vicinity, which is the case here; both curves show a peak positioned at the Fermi level, originating from the presence of the radical, due to the alignment of its SOMO (single occupied molecular orbital) level with the E_F. However, the possible CISS polarization is overshadowed by the radical spin polarization. Furthermore, thermal fluctuations are expected to randomize the orientation of the radical spin.

We simulated this by varying the polar angle across the range [0°, 180°] by rotating steps of 10°. The resulting polarization values around the Fermi level are shown in Fig. 7c. For each rotation angle, the maximum height of the polarization peak at the Fermi level is reported in Fig. 7d (black circles). The average value is approximately zero, indicating that, overall, the CISS effect is not expected to be observed at room temperature, in agreement with the experimental findings reported above. Fig. 7d also shows the peak-height values obtained in the absence of the SOC correction (red squares). Remarkably, the two curves are almost identical, with only a slight shift observed for larger angles. This indicates that, for each angle, the dominant contribution to the spin polarization is not associated with CISS, but rather with the intrinsic spin polarization arising from the presence of the spin of the unpaired electron of the radical. This observation highlights that in the radical systems reported in this work both effects, whether competing or cooperating, are present, but the latter is dominant. To the best of our knowledge, this observation has not been addressed in the previous literature.

3. Conclusions

Two propeller-like conformational enantiomers of PTM radical derivatives having one or two terminal alkyne groups, namely **mPTM** and **bPTM**, have been successfully isolated by CSP-HPLC. Their chiroptical properties have been fully characterized in

solution as well as when structured in drop-cast films, determining the enantiomerization barriers in both scenarios. In solution, no effects of the degree of functionalization (mono- or bis-) were observed obtaining similar results to the racemization barrier previously reported for the non-substituted PTM radical ($\Delta G^{\ddagger}$ = 22 kcal mol^{-1}). On the contrary, a higher racemization barrier, close to the one ascribed to conformationally stable compounds at room temperature, was determined for **mPTM** thin films. Furthermore, for the **bPTM** films, an enhanced barrier ($\geq$24 kcal mol^{-1}) has been measured. The terminal alkyne groups have been exploited as grafting units allowing the preparation of enantioenriched self-assembled monolayers on Au. Spin-dependent electrochemical and charge transport measurements for SAMs of both enantiomers of the **bPTM** radical were conducted without revealing the spin filter effect. Previous reports suggest that the proximity of the SOMO orbital, which carries the radical spin, to the Fermi level of the metal favors the CISS effect,[95] since the spin-polarized current associated with it can be observed at more accessible energies, *i.e.* lower applied bias voltages. However, the absence of CISS is explained here through theoretical analysis, revealing that the contribution of the radical spin polarization dominates, and its thermal fluctuations hinder the possible observation of the CISS contribution. In summary, this work contributes to the field of molecular spintronics by providing insights into the spin-filtering effect in monolayers composed of chiral and paramagnetic organic radicals.

Author contributions

J. A. d. S, P. M-B, J. V and N. C conceived the project and designed the experiments. J. A. d. S and P. M-B performed the chiral separation. J. A. d. S, P. M-B and J. C-T prepared the films and SAMs and performed their characterization. J. A. d. S performed the electrical characterization of EGaIn. S. M-L, A. O and A. G-C performed the chiroptical characterization and the estimation of the racemization barriers. S. M-L performed the DFT calculations for the ECD simulation. L. A. Z and J. J. P performed the electron-transport calculations. J. V and N. C supervised the work. The manuscript was written through contributions of all authors. All authors have given approval to the final version of the manuscript.

Data availability

Data for this article, including the txt, excel, nox files, are available at **https://doi.org/10.20350/digitalCSIC/16351**.

Conflicts of interest

There are no conflicts to declare.

Acknowledgements

The work was supported by Generalitat de Catalunya (2021SGR00443), PID2019-111682RB-I00, PID2022-141393OB-I0, PID2021-127521NB-I00, PID2021-125604NB-I00, PID2019- 109539GB-C43, and PID2022-141712NB-C21 funded by MCIN/AEI/10.13039/501100011033 and ERDF ''A way of making Europe'' and TED2021-131323B-I00 NextGenerationEU, the ''Severo Ochoa'' Programme for Centers of Excellence in R&D FUNFUTURE CEX2019-000917-S through the competitive FUNMAT-FIP-2018 grant and the European Commission – NextGenerationEU (Regulation EU 2020/2094), through CSIC's Quantum Technologies Platform (QTEP). J. C.-T. thanks the DOC-FAM fellowship, grant agreement No. 754397 (H2020-MSCA-COFUND-2016). J. C.-T. is enrolled at the UAB Materials Science PhD program. S. M-L. acknowledges the funding received from the Spanish Junta de Andalucía (DOC 01165). The authors thank the Centro de Servicios de Informática y Redes de Comunicación (CSIRC), UGR, for providing the computing time. L. A. Z. and J. J. P. acknowledge María de Maeztu Program for Units of Excellence in R&D (Grant No. CEX2018-000805-M), Generalitat Valenciana through Programa Prometeo (2021/017) and Centro de Computación Científica of the Universidad Autónoma de Madrid.

References

1 V. Prelog, *Chirality in chemistry*, Nobel Lecture, Switzerland, 1975.
2 Z. Chen, Z. Chi, Y. Sun and Z. Lv, *Chirality*, 2021, **33**, 618.
3 M. Sun, X. Wang, X. Guo, L. Xu, H. Kuang and C. Xu, *Chem. Sci.*, 2022, **13**, 3069.
4 D. Mandler, *Curr. Opin. Electrochem.*, 2018, **7**, 42.
5 H. Kuang, C. Xu and Z. Tang, *Adv. Mater.*, 2020, **32**, 2005110.
6 X. Niu, X. Yang, H. Li, J. Liu, Z. Liu and K. Wang, *Microchim. Acta*, 2020, **187**, 676.
7 L. A. Warning, A. R. Miandashti, L. A. McCarthy, Q. Zhang, C. F. Landes and S. Link, *ACS Nano*, 2021, **15**, 15538.
8 B. Zhao, S. Yang, J. Deng and K. Pan, *Adv. Sci.*, 2021, **8**, 2003681.
9 Z. Li, Z. Mo, S. Meng, H. Gao, X. Niu and R. Guo, *Anal. Methods*, 2016, **8**, 8134.
10 B. Chang, X. Li and T. Sun, *Eur. Polym. J.*, 2019, **118**, 365.
11 G. Zhu, O. J. Kingsford, Y. Yi and K. Wong, *J. Electrochem. Soc.*, 2019, **166**, H205.
12 A. Forment-Aliaga and A. Gaita-Ariño, *J. Appl. Phys.*, 2022, **132**, 180901.
13 C. D. Aiello, J. M. Abendroth, M. Abbas, A. Afanasev, S. Agarwal, A. S. Banerjee, D. N. Beratan, J. N. Belling, B. Berche, A. Botana, J. R. Caram, G. L. Celardo, G. Cuniberti, A. Garcia-Etxarri, A. Dianat, I. Diez-Perez, Y. Guo, R. Gutierrez, C. Herrmann, J. Hihath, S. Kale, P. Kurian, Y. C. Lai, T. Liu, A. Lopez, E. Medina, V. Mujica, R. Naaman, M. Noormandipour, J. L. Palma, Y. Paltiel, W. Petuskey, J. C. Ribeiro-Silva, J. J. Saenz, E. J. G. Santos, M. Solyanik-Gorgone, V. J. Sorger, D. M. Stemer,

J. M. Ugalde, A. Valdes-Curiel, S. Varela, D. H. Waldeck, M. R. Wasielewski, P. S. Weiss, H. Zacharias and Q. H. Wang, *ACS Nano*, 2022, **16**, 4989.
14 A. Chiesa, A. Privitera, E. Macaluso, M. Mannini, R. Bittl, R. Naaman, M. R. Wasielewski, R. Sessoli and S. Carretta, *Adv. Mater.*, 2023, **35**, 2300472.
15 C. Noguez and I. L. Garzón, *Chem. Soc. Rev.*, 2009, **38**, 757.
16 M. P. Moloney, J. Govan, A. Loudon, M. Mukhina and Y. K. Gun'ko, *Nat. Protoc.*, 2015, **10**, 558.
17 H. Huang, L. Hu, Y. Sun, Y. Liu, Z. Kang and D. R. MacFarlane, *Microchim. Acta*, 2019, **186**, 298.
18 R. Raval, *Chem. Soc. Rev.*, 2009, **38**, 707.
19 M. Linares, A. Minoia, P. Brocorens, D. Beljonne and R. Lazzaroni, *Chem. Soc. Rev.*, 2009, **38**, 806.
20 P. Mayorga-Burrezo, J. Muñoz, D. Zaoralová, M. Otyepka and M. Pumera, *ACS Nano*, 2021, **15**, 10067.
21 F. Vera, J. L. Serrano and T. Sierra, *Chem. Soc. Rev.*, 2009, **38**, 781.
22 C. E. Killalea and D. B. Amabilino, *Isr. J. Chem.*, 2021, **61**, 629.
23 C. C. Lee, C. Grenier, E. W. Meijer and A. P. H. J. Schenning, *Chem. Soc. Rev.*, 2009, **38**, 671.
24 B. Shen, Y. Kim and M. Lee, *Adv. Mater.*, 2020, **32**, 1906748.
25 L. Zhang, L. Qin, X. Wang, H. Cao and M. Liu, *Adv. Mater.*, 2014, **26**, 6959.
26 Y. Lu, H. Zhang, Y. Zhu, P. J. Marriott and H. Wang, *Adv. Funct. Mater.*, 2021, **31**, 2101335.
27 Y. Yang, B. Rice, X. Shi, J. R. Brandt, R. Correa Da Costa, G. J. Hedley, D. M. Smilgies, J. M. Frost, I. D. W. Samuel, A. Otero-De-La-Roza, E. R. Johnson, K. E. Jelfs, J. Nelson, A. J. Campbell and M. J. Fuchter, *ACS Nano*, 2017, **11**, 8329.
28 R. Naaman and D. H. Waldeck, *Annu. Rev. Phys. Chem.*, 2015, **66**, 263.
29 P. C. Mondal, P. Roy, D. Kim, E. E. Fullerton, H. Cohen and R. Naaman, *Nano Lett.*, 2016, **16**, 2806.
30 R. Naaman, Y. Paltiel and D. H. Waldeck, *Nat. Rev. Chem.*, 2019, **3**, 250.
31 R. Naaman and D. H. Waldeck, *J. Phys. Chem. Lett.*, 2012, **3**, 2178–2187.
32 O. Ben Dor, N. Morali, S. Yochelis, L. T. Baczewski and Y. Paltiel, *Nano Lett.*, 2014, **14**, 6042.
33 O. Ben Dor, S. Yochelis, S. P. Mathew, R. Naaman and Y. Paltiel, *Nat. Commun.*, 2013, **4**, 2256.
34 G. Koplovitz, D. Primc, O. Ben Dor, S. Yochelis, D. Rotem, D. Porath and Y. Paltiel, *Adv. Mater.*, 2017, **29**, 1606748.
35 A. Stefani, T. Salzillo, P. R. Mussini, T. Benincori, M. Innocenti, L. Pasquali, A. C. Jones, S. Mishra and C. Fontanes, *Adv. Funct. Mater.*, 2024, **34**, 2308948.
36 K. Banerjee-Ghosh, O. Ben Dor, F. Tassinari, E. Capua, S. Yochelis, A. Capua, S. H. Yang, S. S. P. Parkin, S. Sarkar, L. Kronik, L. T. Baczewski, R. Naaman and Y. Paltiel, *Science*, 2018, **360**, 1331.
37 C. Yang, Yi Li, S. Zhou, Y. Guo, C. Jia, Z. Liu, K. N. Houk, Y. Dubi and X. Guo, *Nat. Chem.*, 2023, **15**, 972.
38 L. Scarpetta-Pizo, R. Venegas, P. Barrías, K. Muñoz-Becerra, N. Vilches-Labbé, F. Mura, A. María Méndez-Torres, R. Ramírez-Tagle, A. Toro-Labbé, S. Hevia, J. H. Zagal, R. Oñate, A. Aspée and I. Ponce, *Angew. Chem., Int. Ed.*, 2024, **63**, e202315146.
39 J. M. Abendroth, N. Nakatsuka, M. Ye, D. Kim, E. E. Fullerton, A. M. Andrews and P. S. Weiss, *ACS Nano*, 2017, **11**(7), 7516.
40 J. M. Abendroth, D. M. Stemer, B. P. Bloom, P. Roy, R. Naaman, D. H. Waldeck and P. S. Weiss, *ACS Nano*, 2019, **13**(5), 4928.
41 L. Jia, C. Wang, Y. Zhang, L. Yang and Y. Yan, *ACS Nano*, 2020, **14**(6), 6607.
42 N. Giaconi, L. Poggini, M. Lupi, M. Briganti, A. Kumar, T. K. Das, A. L. Sorrentino, C. Viglianisi, S. Menichetti, R. Naaman, R. Sessoli and M. Mannini, *ACS Nano*, 2023, **17**, 15189.
43 M. Gazzotti, S. Arnaboldi, S. Grecchi, R. Giovanardi, M. Cannio, L. Pasquali, A. Giacomino, O. Abollino and C. Fontanesi, *Electrochim. Acta*, 2018, **286**, 271e278.
44 T. Liu and P. S. Weiss, *ACS Nano*, 2023, **17**(20), 19502.
45 R. Naaman, Y. Paltiel and D. H. Waldeck, *Acc. Chem. Res.*, 2020, **53**, 2659.
46 Z. X. Chen, Y. Li and F. Huang, *Chem*, 2021, **7**, 288.
47 S. Kasemthaveechok, L. Abella, M. Jean, M. Cordier, T. Roisnel, N. Vanthuyne, T. Guizouarn, O. Cador, J. Autschbach, J. Crassous and L. Favereau, *J. Am. Chem. Soc.*, 2020, **142**, 20409.
48 B. D. Gliemann, A. G. Petrovic, E. M. Zolnhofer, P. O. Dral, F. Hampel, G. Breitenbruch, P. Schulze, V. Raghavan, K. Meyer, P. L. Polavarapu, N. Berova and M. Kivala, *Chem. – Asian J.*, 2017, **12**, 31.
49 C. Hirel, J. Pécaut, S. Choua, P. Turek, D. B. Amabilino, J. Veciana and P. Rey, *Eur. J. Org. Chem.*, 2005, 348.
50 Y. Li, W. Zhai, Y. Liao, J. Nie, G. Han, Y. Song, S. Li, J. Hou and Y. Liu, *J. Org. Chem.*, 2019, **84**, 11774.
51 V. M. Tormyshev, A. M. Genaev, G. E. Sal'Nikov, O. Y. Rogozhnikova, T. I. Troitskaya, D. V. Trukhin, V. I. Mamatyuk, D. S. Fadeev and H. J. Halpern, *Eur. J. Org. Chem.*, 2012, 623.
52 W. Zhai, Y. Feng, H. Liu, A. Rockenbauer, D. Mance, S. Li, Y. Song, M. Baldus and Y. Liu, *Chem. Sci.*, 2018, **9**, 4381.
53 P. Mayorga Burrezo, V. G. Jiménez, D. Blasi, I. Ratera, A. G. Campaña and J. Veciana, *Angew. Chem., Int. Ed.*, 2019, **58**, 1628.
54 P. Mayorga-Burrezo, V. G. Jiménez, D. Blasi, T. Parella, I. Ratera, A. G. Campaña and J. Veciana, *Chem. – Eur. J.*, 2020, **26**, 3776.
55 I. Ratera, J. Vidal-Gancedo, D. Maspoch, S. T. Bromley, N. Crivillers and M. Mas-Torrent, *J. Mater. Chem. C*, 2021, **9**, 10610.
56 J. Irurre, J. Santamaría and M. Concepción González-Rego, *Chirality*, 1995, **7**, 154.
57 F. Grillo, V. Mugnaini, M. Oliveros, S. M. Francis, D. J. Choi, M. V. Rastei, L. Limot, C. Cepek, M. Pedio, S. T. Bromley, N. V. Richardson, J. P. Bucher and J. Veciana, *J. Phys. Chem. Lett.*, 2012, **3**, 1559.
58 D. Gutiérrez, S. Riera-Galindo, M. R. Ajayakumar, J. Veciana, C. Rovira, M. Mas-Torrent and N. Crivillers, *J. Phys. Chem. C*, 2018, **122**, 17784.

59 N. Crivillers, M. Mas-Torrent, S. Perruchas, N. Roques, J. Vidal-Gancedo, J. Veciana, C. Rovira, L. Basabe-Desmonts, B. J. Ravoo, M. Crego-Calama and D. N. Reinhoudt, *Angew. Chem., Int. Ed.*, 2007, **46**, 2215.
60 M. Mas-Torrent, N. Crivillers, C. Rovira and J. Veciana, *Chem. Rev.*, 2012, **112**, 2506.
61 T. Junghoefer, E. M. Nowik-Boltyk, J. A. De Sousa, E. Giangrisostomi, R. Ovsyannikov, T. Chassé, J. Veciana, M. Mas-Torrent, C. Rovira, N. Crivillers and M. B. Casu, *Chem. Sci.*, 2020, **11**, 9162.
62 N. Crivillers, M. Paradinas, M. M. Torrent, S. T. Bromley, C. Rovira, C. Ocal and J. Veciana, *Chem. Commun.*, 2011, **47**, 4664.
63 L. Yuan, C. Franco, N. Crivillers, M. Mas-Torrent, L. Cao, C. S. S. Sangeeth, C. Rovira, J. Veciana and C. A. Nijhuis, *Nat. Commun.*, 2016, **7**, 12066.
64 F. Bejarano, I. J. Olavarria-Contreras, A. Droghetti, I. Rungger, A. Rudnev, D. Gutiérrez, M. Mas-Torrent, J. Veciana, H. S. J. Van Der Zant, C. Rovira, E. Burzurí and N. Crivillers, *J. Am. Chem. Soc.*, 2018, **140**, 1691.
65 J. A. De Sousa, R. Pfattner, D. Gutiérrez, K. Jutglar, S. T. Bromley, J. Veciana, C. Rovira, M. Mas-Torrent, B. Fabre and N. Crivillers, *ACS Appl. Mater. Interfaces*, 2023, **15**, 4635.
66 J. A. De Sousa, F. Bejarano, D. Gutiérrez, Y. R. Leroux, E. M. Nowik-Boltyk, T. Junghoefer, E. Giangrisostomi, R. Ovsyannikov, M. B. Casu, J. Veciana, M. Mas-Torrent, B. Fabre, C. Rovira and N. Crivillers, *Chem. Sci.*, 2020, **11**, 516.
67 S. Zhang, K. L. Chandra and C. B. Gorman, *J. Am. Chem. Soc.*, 2007, **129**, 4876.
68 P. Pla-Vilanova, A. C. Aragonès, S. Ciampi, F. Sanz, N. Darwish and I. Diez-Perez, *Nanotechnology*, 2015, **26**, 381001.
69 T. Zaba, A. Noworolska, C. M. Bowers, B. Breiten, G. M. Whitesides and P. Cyganik, *J. Am. Chem. Soc.*, 2014, **136**, 11918.
70 P. Peluso, B. Sechi, G. Lai, A. Dessì, R. Dallocchio, S. Cossu, E. Aubert, R. Weiss, P. Pale, V. Mamane and B. Chankvetadze, *J. Chromatogr. A*, 2020, **1625**, 461303.
71 V. Diez-Cabanes, G. Seber, C. Franco, F. Bejarano, N. Crivillers, M. Mas-Torrent, J. Veciana, C. Rovira and J. Cornil, *ChemPhysChem*, 2018, **19**, 2572.
72 E. Yashima, K. Maeda, O. Trapp, N. Berova, S. Collina and G. Pescitelli, *Chirality*, 2022, **34**, 699.
73 C. Yamamoto, E. Yashima and Y. Okamoto, *J. Am. Chem. Soc.*, 2002, **124**, 12583.
74 Y. Okamoto and T. Ikai, *Chem. Soc. Rev.*, 2008, **37**, 2593.
75 I. Ali, M. Suhail, Z. A. Alothman and A. Alwarthan, *Chirality*, 2017, **29**, 386.
76 K. J. Weiland, T. Brandl, K. Atz, A. Prescimone, D. Häussinger, T. Šolomek and M. Mayor, *J. Am. Chem. Soc.*, 2019, **141**, 2104.
77 J. Veciana and M. I. Crespo, *Angew. Chem., Int. Ed. Engl.*, 1991, **30**, 74.
78 P. Osswald and F. Würthner, *J. Am. Chem. Soc.*, 2007, **129**, 14319.
79 C. Wolf, *Chem. Soc. Rev.*, 2005, **34**, 595.
80 M. Rickhaus, L. Jundt and M. Mayor, *Chimia*, 2016, **70**, 192.
81 P. Ravat, *Chem. – Eur. J.*, 2021, **27**, 3957.
82 B. Driesschaert, R. Robiette, F. Lucaccioni, B. Gallez and J. Marchand-Brynaert, *Chem. Commun.*, 2011, **47**, 4793.
83 Y. Vaynzof, *Adv. Energy Mater.*, 2020, **10**, 2003073.
84 D. M. Taylor, *Semicond. Sci. Technol.*, 2015, **30**, 054002.
85 Y. Diao, L. Shaw, Z. Bao and S. C. B. Mannsfeld, *Energy Environ. Sci.*, 2014, **7**, 2145.
86 L. Zhao, X. Ren and X. Yan, *CCS Chem.*, 2021, **3**, 678.
87 M. A. Medel, C. M. Cruz, D. Miguel, V. Blanco, S. P. Morcillo and A. G. Campaña, *Angew. Chem., Int. Ed.*, 2021, **60**, 22051.
88 M. A. Medel, R. Tapia, V. Blanco, D. Miguel, S. P. Morcillo and A. G. Campaña, *Angew. Chem., Int. Ed.*, 2021, **133**, 6159.
89 A. J. Bard and L. R. Faulkner, *Electrochemical Methods; Fundamentals and Applications*, John Wiley & Sons, Ltd, 2002.
90 A. L. Eckermann, D. J. Feld, J. A. Shaw and T. J. Meade, *Coord. Chem. Rev.*, 2010, **254**, 1769.
91 P. C. Mondal, C. Fontanesi, D. H. Waldeck and R. Naaman, *ACS Nano*, 2015, **9**, 3377.
92 R. Torres-Cavanillas, G. Escorcia-Ariza, I. Brotons-Alcázar, R. Sanchis-Gual, P. C. Mondal, L. E. Rosaleny, S. Giménez-Santamarina, M. Sessolo, M. Galbiati, S. Tatay, A. Gaita-Ariño, A. Forment-Aliaga and S. Cardona-Serra, *J. Am. Chem. Soc.*, 2020, **142**, 17572.
93 N. Vogel, J. Zieleniecki and I. Köper, *Nanoscale*, 2012, **4**, 3820.
94 A. Alessandrini, C. A. Bortolotti, G. Bertoni, A. Vezzoli and P. Facci, *J. Phys. Chem. C*, 2008, **112**, 3747.
95 W. Dednam, M. A. García-Blázquez, L. A. Zotti, E. B. Lombardi, C. Sabater, S. Pakdel and J. J. Palacios, *ACS Nano*, 2023, **17**, 6452.
96 A. M. Ortuño, P. Reiné, L. Álvarez de Cienfuegos, I. R. Márquez, W. Dednam, E. B. Lombardi, J. J. Palacios, E. Leary, G. Longhi, V. Mujica, A. Millán, M. T. González, L. A. Zotti, D. Miguel and J. M. Cuerva, *Angew. Chem., Int. Ed.*, 2023, **62**, e2022186.
97 M. A. García-Blázquez, W. Dednam and J. J. Palacios, *J. Phys. Chem. Lett.*, 2023, **14**, 7931.

